Nanoscale

COMMUNICATION

View Article Online
View Journal | View Issue

Cite this: *Nanoscale*, 2019, **11**, 14113

Received 19th May 2019,
Accepted 12th July 2019

DOI: 10.1039/c9nr04264d

rsc.li/nanoscale

Tin diselenide van der Waals materials as new candidates for mid-infrared waveguide chips

Mengfei Xue,[a,b] Qi Zheng,[a,b] Runkun Chen,[a,b] Lihong Bao,*[a,b,c] Shixuan Du[a,b,c] and Jianing Chen*[a,b,c]

Mid-infrared is a spectral region of molecular vibration and rotation modes and thus, it has been widely used in chem/bio analysis. On-chip MIR waveguides combining attenuated total reflection spectroscopy provide an efficient way to minimize equipment size and benefit chemical trace analysis. But, inevitable surface roughness-induced scattering is harmful for waveguide mode propagation in traditional sensors. Two-dimensional materials are natural thin slabs with atomic-scale smooth surfaces and thus could be excellent for building weak surface scattering waveguides. Here, we used near-field microscopy to investigate a waveguide mode of 1T tin diselenide slabs at nanoscale resolution in 5.13–6.57 μm and manipulate the mode strengths and wavelengths by controlling the slab thickness. This work extends two-dimensional materials as building blocks for integrated MIR chips.

Introduction

Mid-infrared (MIR) spectroscopy in the range of 2.5–20 μm can induce vibrational and rotational excitation of organic and inorganic molecules and provide precision recognition of chemical and structural information. Hence, MIR spectroscopy is widely used in chemical and biological analyses.[1–4] However, due to their large size, most MIR spectrometers are still confined to laboratories. An on-chip integration sensor[5,6] is conducive to miniaturizing MIR sensing systems as well as being able to directly achieve chemical information from samples compared with plasmonic sensors which rely on sensitivity to surrounding refractive indices of Fano resonance.[7,8] Previous works of MIR dielectric waveguides combining attenuated total reflection (ATR) spectroscopy[9] significantly minimized sensor volume. Most materials possess vibrational transition and thus only a few materials such as mercury-cadmium-telluride,[10] germanium,[11] silicon,[12] and diamond[13] are suitable candidates for a MIR waveguide. For traditional waveguides, scattering radiation introduced by surface roughness causes the major source of intrinsic damping, which is harmful for waveguide mode propagation, but an actual fabrication procedure can't make perfectly smooth surfaces. Due to their two-dimensional structure, 2D materials are natural slabs with atomically smooth surfaces and thus could be potential media to build low-surface-scattering-loss MIR waveguides.

Tin diselenide ($SnSe_2$) is a semiconductor belonging to 1T MX_2 (M – metal, X – chalcogen) 2D crystals with about a 1.0 eV bulk bandgap. In-plane and out-of-plane dielectric constants of $SnSe_2$ are 10.7 and 9.42, respectively. Due to its low cost and superior optical and electronic properties, $SnSe_2$ has great application potential in solar cells and atomic electronics.[14] Waveguide modes of van der Waals (vdW) materials have been investigated by scanning near-field optical microscopy with a sharp metal or fiber tip in near-infrared and visible regions.[15,16] In previous studies, 2D materials were discovered to support polariton modes. For example, graphene was found to support surface plasmon.[17,18] Thin plates of hexagonal boron nitride (h-BN) and α-MoO_3 were discovered to support hyperbolic phonon polaritons with high confinement.[19,20] Transition metal dichalcogenides (TMD) were proven to support exciton–polariton,[21] ordinary and extraordinary waveguide modes introduced by optical anisotropy.[15] In this work, by using scattering type scanning near-field optical microscopy (s-SNOM) combined with a tunable quantum cascade laser, we systematically investigated edge launching waveguide modes of a $SnSe_2$ slab in a MIR range (5.13–6.57 μm). IR imaging directly shows sensitive manipulations of waveguide strength and wavelength by changing a slab's thickness. In addition, we used CMOSOL multiphysics to perform numerical simulations of planar waveguides, and calculated results which were consistent with experimental observations. Our work opens a new avenue to use 2D vdW materials in chem/bio sensing area.

[a]*Institute of Physics, Chinese Academy of Sciences and Beijing National Laboratory for Condensed Matter Physics, P.O. Box 603, Beijing, 100190, China*
[b]*School of Physical Sciences, University of Chinese Academy of Sciences, Beijing 100049, China*
[c]*Songshan Lake Materials Laboratory, Dongguan 523808, China.*
E-mail: jnchen@iphy.ac.cn, lhbao@iphy.ac.cn

Results and discussion

S-SNOM is based on a tapping mode atomic force microscope (AFM) and demodulating the near-field signal at higher harmonics of the tip vibration frequency. Combining pseudo-heterodyne detection, s-SNOM allowed us to simultaneously obtain topography and background-free near-field features. In this work, we chose a third-order harmonics near-field amplitude signal to exhibit the waveguide mode of a $SnSe_2$ slab. Fig. 1a shows the schematic of experimental configuration; the parabolic mirror is used to focus incident light and collect the scattered signal. Unlike situations of surface plasmon polariton and hyperbolic phonon polariton, motivation of a waveguide mode in $SnSe_2$ does not need an optical antenna to overcome momentum mismatch. A laser could directly couple into a planar waveguide through edge scattering.[16,22]

Former studies of TMD materials showed that a waveguide mode is launched from the AFM tip and the near-field fringe is an interference between tip-scattered light and part of the waveguide mode which converted into photons at the edge.[15,21] But, in our work, the edges of $SnSe_2$ slabs scattered a laser beam and efficiently launched a waveguide mode as shown in Fig. 1a. First, we measured a 347 nm thick $SnSe_2$ slab from ω = 1620 cm^{-1} to 1870 cm^{-1}. In Fig. 1b the red arrow indicates the projection of laser incidence direction, which is perpendicular to edge A. Two fringe patterns appear parallel to edges A and B, respectively. To verify the fringes were launched by an AFM tip or edge, we changed the laser illumination conditions. As shown in Fig. 1c, we set the laser projection parallel to edge A and the corresponding near-field image only shows the fringe parallel to edge A while the fringe parallel to edge B disappeared. A tip launching mode should not be affected by changing illumination configurations. Thus, an AFM tip is excluded as a launcher. Fig. 1d shows the period of fringe parallel to edge A at different illumination conditions, which is 2.9 μm from Fig. 1b and 3 μm from Fig. 1c, respectively. Fringe periods are comparable to a laser wavelength λ_0 = 5.35 μm. Thus, we believe the fringe pattern is a waveguide mode and the fringe period should be a waveguide wavelength. In our experimental configuration, the laser is focused on the probe tip with a focal spot about 20 μm × 40 μm and the angle between the laser incidence direction and sample plane is about 30 degrees. Considering different illumination configurations, the laser spot could not fully cover one or more edges when the inner sample is under the tip during a scanning process; thus, in Fig. 1c, the fringe pattern parallel to edge B doesn't appear. To further verify the near-field patterns are launched by edges, we moved the laser spot by slightly changing the position of its parabolic mirror to let the laser shine on edge C in Fig. 1e. Compared to Fig. 1f, we clearly observed the fringe parallel to edge C when edge C was illuminated in Fig. 1g. This observation unambiguously confirms edges of

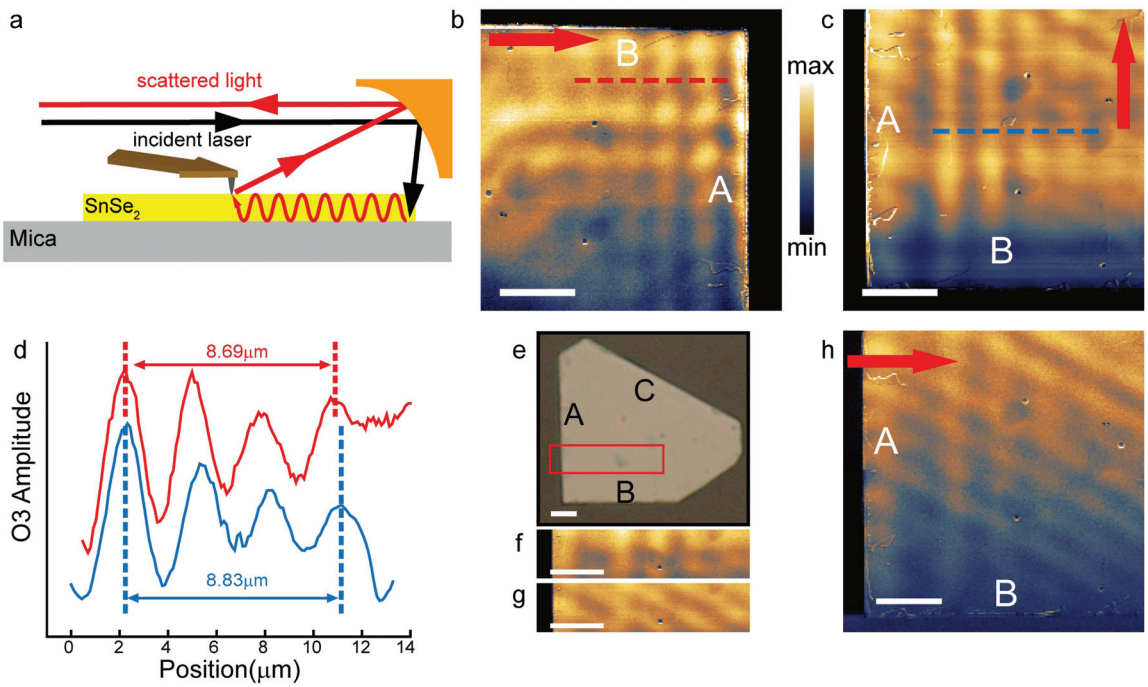

Fig. 1 Scale bars of all near-field amplitude and optical microscope images are 5 μm, red arrows of near-field images indicate projection of laser incident direction. (a) Schematic of s-SNOM configuration. $SnSe_2$ slab edge scatters the laser and subsequently emits waveguide mode. (b) Near-field images of $SnSe_2$ slabs at ω = 1870 cm^{-1}, projection of laser is perpendicular to edge A. (c) Near-field images of $SnSe_2$ slabs at ω = 1870 cm^{-1}, projection of laser is parallel to edge A. (d) Fringe profiles at ω = 1870 cm^{-1}, red and blue curves corresponding to dashed lines in (b and c), respectively. (e) Optical image of $SnSe_2$ slab, thickness of $SnSe_2$ is 347 nm. (f)–(g) Near-field images at ω = 1620 cm^{-1} of red frame in (e) before and after moving laser spot to illuminate edge C. Fringe parallel to C emerges when edge C is illuminated. (h) Near-field image at ω = 1720 cm^{-1} of slab with edge C illuminated.

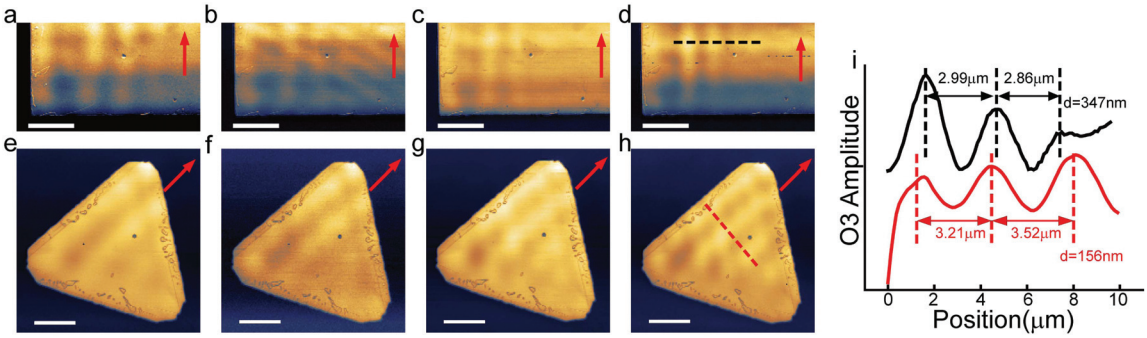

Fig. 2 Scale bars of all near-field amplitude images are 5 μm; red arrows of near-field images indicate projection of laser incident direction. (a)–(d) Near-field images of 347 nm thick $SnSe_2$ slab at ω = 1570 cm^{-1}, 1720 cm^{-1}, 1830 cm^{-1} and 1920 cm^{-1}, respectively. (e)–(h) Near-field images of 156 nm thick $SnSe_2$ slabs at ω = 1570 cm^{-1}, 1720 cm^{-1}, 1830 cm^{-1} and 1920 cm^{-1}, respectively. (i) Fringe profiles taken from dashed lines in (d and h) at 1920 cm^{-1}.

$SnSe_2$ flakes are launchers of inner electromagnetic waves. The effects of phonon and carrier can be safely neglected because their response frequencies are far below the experimental region. In Fig. 1h, the fringe parallel to edge C transmitted more (as far as nearly 20 μm, almost to the corner of edges A and B). Compared with a graphene plasmon, which requires critical conditions such as close lattice matching material for substrate and low temperature environment to reach 10 μm propagation distance,[23] the waveguide mode found in $SnSe_2$ indicates it is a good MIR transmission medium.

Previous research indicates a waveguide mode could be manipulated by changing core layer thickness.[24,25] We then investigated the variation of mode wavelength at different slab thicknesses. We placed slabs properly to let the laser incident direction be parallel to one edge. In this configuration, the edge could be fully illuminated during the entire scanning process. Fig. 2a–d and e–h show near-field images of 347 nm and 156 nm thick samples, respectively; red arrows indicate the laser incidence direction, and fringes are clear on both slabs under laser frequencies from ω = 1570 cm^{-1} to 1920 cm^{-1}. Fig. 2i shows fringe profiles of two slabs taken from the dashed line in Fig. 2d and h at ω = 1920 cm^{-1}, respectively. The wavelength of the guide mode is shorter for the thicker sample, which is 3.37 μm for the 156 nm thick slab and 2.97 μm for the 347 nm thick slab. Decreasing of waveguide wavelengths with increasing $SnSe_2$ slab thickness also exists under other frequencies as shown in Fig. 2a–h.

Comparing near-field images of 156 nm and 347 nm thick samples, we also found that fringe contrast was stronger for the 347 nm thick slab. Thus, we selected $SnSe_2$ slabs with different thicknesses ranging from 47 nm to 233 nm to investigate mode contrast. Fig. 3a–e show near-field images of $SnSe_2$ slabs with different thicknesses at ω = 1950 cm^{-1}. For the d = 47 nm slab in Fig. 3a, we barely recognized the waveguide fringe. For the d = 85 nm slab in Fig. 3b, a fringe pattern starts to emerge. When slab thickness becomes larger than 100 nm the fringe appears more and more clearly with increasing thickness; *e.g.*, in Fig. 3c–e IR imaging indicates thicker slabs (*i.e.*, more than 100 nm) are suitable to fabricate a sensor chip because of stronger electromagnetic field confinement in thicker slabs. To explain the change of fringe contrast and periods at different slabs thicknesses, we carried out COMSOL calculations to reproduce electromagnetic field of cladding and core layers. Calculated results indicated that the near-field fringe of $SnSe_2$ is the TE_0 mode. Fig. 4a–c and d–f show Ez field distributions of three $SnSe_2$ slabs with different thicknesses of d = 120 nm, d = 230 nm and d = 340 nm at ω = 1520 cm^{-1} and ω = 1950 cm^{-1}, respectively; the y axis is normal to the slab surface and the x axis indicates the direction of waveguide transmission. From Fig. 4a and d we can see that for the d = 120 nm slab, the Ez field distributes deeply into the mica substrate. When the slab becomes thicker, electric fields are confined in the slab and less electric field distributes in mica as shown in Fig. 4a–c and d–f. We believe weak

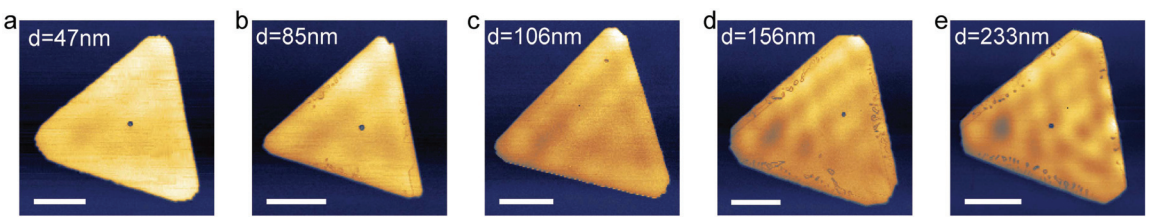

Fig. 3 Scale bars of all near-field amplitude images are 5 μm. (a)–(e), Near-field amplitude images at ω = 1950 cm^{-1} of five $SnSe_2$ slabs with different thicknesses ranging from 47 nm to 233 nm. The Near-field images exhibit stronger fringe contrast and shorter guide mode wavelengths for thicker slabs.

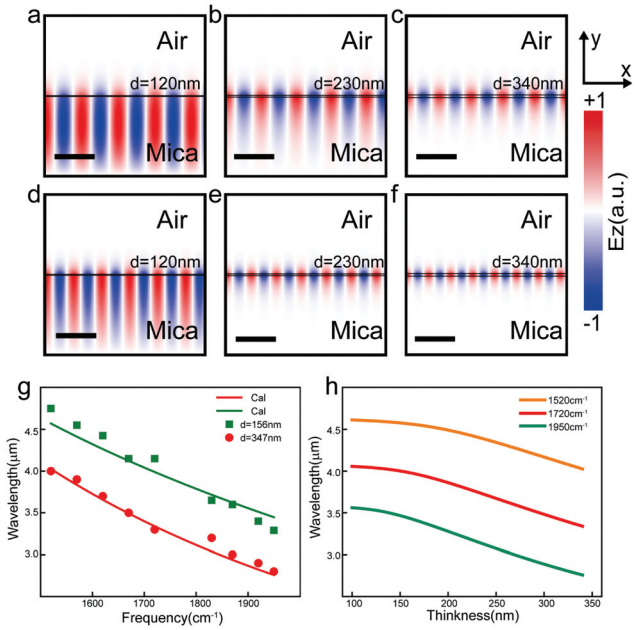

Fig. 4 Simulation results of $SnSe_2$ slab waveguide modes. Scale bars of electric field distribution images are 5 μm. Calculation results show stronger field confinement and shorter guide mode wavelengths in thicker slabs. (a)–(c) Ez distribution at ω = 1520 cm^{-1} of 120 nm, 230 nm, 340 nm thick $SnSe_2$ slabs. (d)–(f) Ez distribution at ω = 1950 cm^{-1} of 120 nm, 230 nm, 340 nm thick slabs. (g) Dispersion relation of 347 nm and 156 nm thick slabs. Symbols are data, solid lines are calculated results. Refractive index of mica is set 1.45 in our model. (h) Calculated results of variation tendency of waveguide wavelengths with slab thickness changes at ω = 1520 cm^{-1}, 1720 cm^{-1} and 1950 cm^{-1}.

confinement of the Ez field in a core layer causes weak fringe contrast in thin slabs. Moreover, Fig. 4a–c and d–f also show that mode wavelengths decrease when slabs become thicker, which is consistent with experimental results in Fig. 2. Fig. 4g shows dispersion relations of d = 156 nm and 347 nm slabs; the calculated result is highly consistent with experimental data. The refractive index of mica measured before is 1.58–1.61 but, by setting refractive index at 1.45, we could get good agreement between calculated and experimental results. A slight change of mica's refractive index was acceptable as we performed experiments in the MIR region. Calculated and experimental results showed that changing thickness of a $SnSe_2$ slab could efficiently and sensitively modify the electric field distribution and waveguide wavelengths.

Conclusions

In conclusion, we systematically investigated MIR waveguide modes in $SnSe_2$ slabs. By using s-SNOM, we have overcome the diffraction limit and directly observed the edge launching a TE_0 mode fringe. We have experimentally and theoretically shown that mode wavelength and strength could be efficiently manipulated by changing the slab thickness. Our work indicates that $SnSe_2$ could be an effective waveguide in the MIR region and extends vdW materials with atomic-scale smooth surfaces as potential building blocks for MIR sensor chips.

Materials and methods

Synthesis of $SnSe_2$

$SnSe_2$ slabs were synthesized in a CVD reactor. During the growth process, one quartz boat containing ~15 mg SnI_2 powder was placed in the centre of the tubular furnace, and another quartz boat containing ~200 mg Se powder was placed at the upper inlet of the furnace. Temperature was ~530 °C with the SnI_2 powder and ~440 °C with Se powder. A 20% H_2/Ar gas was used as carrier gas with 50 sccm gas flow at ambient atmosphere. Deposition temperatures were in a range of 280–420 °C relying on the different positions of the mica substrate.

Conflicts of interest

There are no conflicts to declare.

Acknowledgements

This work was supported by the National Key Research and Development Program of China (2016YFA0203500, 2016YFA0202300), National Natural Science Foundation of China (Grant No.11874407), and Strategic Priority Research Program of Chinese Academy of Sciences (Grant No. XDB 30000000).

Notes and references

1 S. Hou, C. B. Riley, C. A. Mitchell, R. A. Shaw, J. Bryanton, K. Bigsby and J. T. McClure, *Talanta*, 2015, **142**, 110–119.
2 R. Pandey, N. C. Dingari, N. Spegazzini, R. R. Dasari, G. L. Horowitz and I. Barman, *TrAC, Trends Anal. Chem.*, 2015, **64**, 100–108.
3 M. Kansiz, H. Billman-Jacobe and D. McNaughton, *Appl. Environ. Microbiol.*, 2000, **66**, 3415–3420.
4 M. C. Estevez, M. Alvarez and L. M. Lechuga, *Laser Photonics Rev.*, 2012, **6**, 463–487.
5 M. Sieger and B. Mizaikoff, *Anal. Chem.*, 2016, **88**, 5562–5573.
6 J. Haas and B. Mizaikoff, *Rev. Anal. Chem.*, 2016, **9**, 45–68.
7 Y. Wang, C. Sun, H. Li, Q. Gong and J. Chen, *Nanoscale*, 2017, **9**, 11085–11092.
8 J. Chen, F. Gan, Y. Wang and G. Li, *Adv. Opt. Mater.*, 2018, **6**, 1701152.
9 B. Mizaikoff, *Anal. Chem.*, 2003, **75**, 258A–267A.
10 X. Wang, J. Antoszewski, G. Putrino, W. Lei, L. Faraone and B. Mizaikoff, *Anal. Chem.*, 2013, **85**, 10648–10652.

11 Y. C. Chang, V. Paeder, L. Hvozdara, J. M. Hartmann and H. P. Herzig, *Opt. Lett.*, 2012, **37**, 2883–2885.
12 M. Muneeb, X. Chen, P. Verheyen, G. Lepage, S. Pathak, E. Ryckeboer, A. Malik, B. Kuyken, M. Nedeljkovic, J. Van Campenhout, G. Z. Mashanovich and G. Roelkens, *Opt. Express*, 2013, **21**, 11659–11669.
13 X. Wang, M. Karlsson, P. Forsberg, M. Sieger, F. Nikolajeff, L. Osterlund and B. Mizaikoff, *Anal. Chem.*, 2014, **86**, 8136–8141.
14 R. Y. Wang, M. A. Caldwell, R. G. D. Jeyasingh, S. Aloni, R. M. Shelby, H. S. P. Wong and D. J. Milliron, *J. Appl. Phys.*, 2011, **109**, 113506.
15 D. Hu, X. Yang, C. Li, R. Liu, Z. Yao, H. Hu, S. N. G. Corder, J. Chen, Z. Sun, M. Liu and Q. Dai, *Nat. Commun.*, 2017, **8**, 1471.
16 D. Wintz, K. Chaudhary, K. Wang, L. A. Jauregui, A. Ambrosio, M. Tamagnone, A. Y. Zhu, R. C. Devlin, J. D. Crossno, K. Pistunova, K. Watanabe, T. Taniguchi, P. Kim and F. Capasso, *ACS Photonics*, 2018, **5**, 1196–1201.
17 J. Chen, M. Badioli, P. Alonso-Gonzalez, S. Thongrattanasiri, F. Huth, J. Osmond, M. Spasenovic, A. Centeno, A. Pesquera, P. Godignon, A. Zurutuza Elorza, N. Camara, F. J. G. de Abajo, R. Hillenbrand and F. H. L. Koppens, *Nature*, 2012, **487**, 77–81.
18 Z. Fei, A. S. Rodin, G. O. Andreev, W. Bao, A. S. McLeod, M. Wagner, L. M. Zhang, Z. Zhao, M. Thiemens, G. Dominguez, M. M. Fogler, A. H. C. Neto, C. N. Lau, F. Keilmann and D. N. Basov, *Nature*, 2012, **487**, 82–85.
19 S. Dai, Z. Fei, Q. Ma, A. S. Rodin, M. Wagner, A. S. McLeod, M. K. Liu, W. Gannett, W. Regan, K. Watanabe, T. Taniguchi, M. Thiemens, G. Dominguez, A. H. C. Neto, A. Zettl, F. Keilmann, P. Jarillo-Herrero, M. M. Fogler and D. N. Basov, *Science*, 2014, **343**, 1125–1129.
20 Z. Zheng, J. Chen, Y. Wang, X. Wang, X. Chen, P. Liu, J. Xu, W. Xie, H. Chen, S. Deng and N. Xu, *Adv. Mater.*, 2018, **30**, 1705318.
21 F. Hu, Y. Luan, M. E. Scott, J. Yan, D. G. Mandrus, X. Xu and Z. Fei, *Nat. Photonics*, 2017, **11**, 356.
22 N. Chandrasekhar, S. Basak, M. A. Mohiddon and R. Chandrasekar, *ACS Appl. Mater. Interfaces*, 2014, **6**, 1488–1494.
23 G. X. Ni, A. S. McLeod, Z. Sun, L. Wang, L. Xiong, K. W. Post, S. S. Sunku, B. Y. Jiang, J. Hone, C. R. Dean, M. M. Fogler and D. N. Basov, *Nature*, 2018, **557**, 530–533.
24 J. T. Bradshaw, S. B. Mendes and S. S. Saavedra, *Anal. Chem.*, 2005, **77**, 28a–36a.
25 S. B. Mendes and S. S. Saavedra, *Appl. Opt.*, 2000, **39**, 612–621.